AIMS Biophysics

AIMS Biophysics, 13(2): 131−142.
DOI: 10.3934/biophy.2026008
Received: 21 November 2025
Revised: 11 March 2026
Accepted: 20 March 2026
Published: 27 March 2026

http://www.aimspress.com/journal/biophysics

Research article

Subtomogram averaging by cryo electron tomography using CRYO ARM™ 300 II for purified and cellular samples

Fumiaki Makino[1,2,3,*], Haruaki Yanagisawa[4], Fabian Eisenstein[4,5], Tomoko Miyata[2,3], Miki Kinoshita[2,3], Masahide Kikkawa[4] and Keiichi Namba[2,3,*]

[1] JEOL Ltd., Akishima, Tokyo 196-8558, Japan
[2] Graduate School of Frontier Biosciences, The University of Osaka, Suita, Osaka 565-0871, Japan
[3] JEOL YOKOGUSHI Research Alliance Laboratories, The University of Osaka, Suita, Osaka 565-0871, Japan
[4] Department of Cell Biology and Anatomy, Graduate School of Medicine, The University of Tokyo, Tokyo 113-0033, Japan
[5] Present address: DECTRIS AG, 5405 Baden-Daettwil, Switzerland

* **Correspondence:** Email: fumakino@jeol.co.jp, namba.keiichi.fbs@osaka-u.ac.jp; Tel: +81425422227, +81668794625.

Abstract: Cryo electron tomography (cryo-ET) enables three-dimensional visualization of biological macromolecules in their near-native environments, bridging the gap between structural and cellular biology. In this study, we evaluated high-resolution subtomogram averaging (STA) using a cryo-TEM (CRYO ARM™ 300 II, JEOL) and PACEtomo software system for both single-particle analysis (SPA) type grids and lamellae prepared by cryo-focused ion beam (cryo-FIB) milling (JIB-4700F, JEOL). Using mouse apoferritin and *E. coli* ribosomes in thin vitreous ice film, resolutions of 2.04 Å and 2.86 Å were achieved, respectively. Using cryo-FIB lamellae of *Salmonella* cells, in situ ribosome structures were resolved to 8.2 Å resolution.

Keywords: cryo-EM; cryo-ET; STA; cryo-FIB-SEM; CryoLameller; CRYO ARM; structural cell biology

1. Introduction

One of the major challenges in life sciences is understanding complex biological mechanisms based on the structure, dynamics, and interactions of macromolecules. To achieve this, it is essential to visualize the three-dimensional structures of a wide variety of macromolecular complexes involved in biological functions and to elucidate their spatial relationships. Considering the complexity of cells, the number of molecular assemblies that must be visualized is estimated to range from hundreds of millions to tens of billions.

Cryo electron microscopy (cryo-EM) using transmission cryo electron microscopes (cryo-TEM), which was awarded the Nobel Prize in Chemistry in 2017, revolutionized structural biology by enabling high-resolution structure determination without the need for crystallization through advances in single-particle analysis (SPA). Meanwhile, cryo electron tomography (cryo-ET), which has recently attracted significant attention, allows direct three-dimensional observation of samples in a vitrified state. This technique enables visualization of biomolecules in cells and tissues in near-native states and allows three-dimensional reconstruction of ribosomes, membrane protein complexes, cytoskeletal structures, and virus particles within their physiological environments [1]. As a result, cryo-ET has become a core technology driving the progress of structural cell biology.

In electron tomography, samples are imaged sequentially in multiple tilt angles, and three-dimensional structures are reconstructed from the resulting set of two-dimensional projections. Furthermore, subtomogram averaging (STA), in which similar structures within tomograms are extracted and averaged, has made it possible to achieve resolutions comparable to SPA. However, STA is still not a routine approach. Achieving such high resolutions generally requires substantial expertise of the analyst and the combined use of multiple complementary processing strategies [2]. Several factors, such as electron beam irradiation damage and sample thickness, still limit the achievable resolution. To overcome these limitations, the development of advanced microscopes with highly stable electron optics, automated and efficient data acquisition software, and highly-sensitive, fast direct electron detectors has progressed rapidly. In recent years, advances in cryo-focused ion beam-scanning electron microscopy (cryo-FIB-SEM) technology have made it possible to selectively thin specific regions of vitrified cells and tissues into lamellae with thicknesses suitable for transmission electron microscopy imaging (approximately 100 - 200 nm). This innovation enables in situ structural analysis of thick cellular and tissue samples that were previously inaccessible to transmission electron microscopy, thereby greatly expanding the applicability of cryo-ET [3,4].

In this study, tomographic data acquisition and subtomogram averaging analyses were performed using a cryo-TEM (CRYO ARM^{TM} 300 II, JEOL) and PACEtomo [5] system for both SPA-type thin vitreous ice grids and lamella samples prepared with a cryo-FIB-SEM (JIB-4700F, JEOL). From the obtained structural information, we evaluated the reproducibility and versatility of high-resolution structural analysis by cryo-ET and assessed its potential for further practical improvement in resolution.

2. Materials and methods

2.1. Stage motion analysis using tomographic acquisition

To quantitatively evaluate stage behavior during tomographic data acquisition with CRYO ARM^{TM} 300 II, the stage position changes were analyzed during tilting using the special cartridge

system of CRYO ARM™. The stage coordinate system consists of Stage X, Y, and Z. The longitudinal axis of the cartridge corresponds to Stage Y, which is equivalent to the tilt axis during tomographic acquisition, and Stage X is oriented perpendicular to the tilt axis. Stage Z represents the specimen height direction (Figure 1A).

Tomographic data were acquired using a built-in tomography function in SerialEM, employing a dose-symmetric acquisition scheme covering a tilt range from −60° to +60°. Specifically, tilting was performed starting from 0°, using a scheme in which two tilt angles were grouped as a unit (e.g., 0 → −3 → −6 → +3 → +6 → −9 → −12 → …). A total of 41 independent tilt series were acquired, of which nine datasets were selected for detailed analysis. For each tilt angle, the positions of Stage X and Stage Y were recorded. Mean values and standard deviations (SD) were calculated for each tilt angle to evaluate lateral stage displacements.

In addition, changes in the specimen height associated with tilting were evaluated by analyzing the Stage Z component. For each tilt angle, the measured defocus value (nominally set to −8 μm) was referenced to the value at 0° tilt, and the resulting difference was treated as a relative displacement along the Z direction. This analysis enabled quantitative evaluation and graphical visualization of tilt-angle-dependent changes in specimen height during tomographic acquisition.

2.2. Sample preparation of SPA-type grid for cryo-ET

Mouse apoferritin was expressed and purified following the same method described previously [5]. *E. coli* 70S ribosome was prepared as previously described [6]. For both apoferritin and ribosome samples, Quantifoil R1.2/1.3 200-mesh grids were gold sputter coated using an AT-900 multi-coater (ATA Inc., Japan) and rendered hydrophilic by glow discharge using a PIB-10 ion bombarder (Vacuum Device Inc., Japan), and 3 μL solutions were applied on the grids. The grids were blotted for 3 s and immediately plunge-frozen in liquid ethane using Vitrobot™ (Thermo Fisher Scientific).

2.3. Cryo-ET data collection and STA image analysis of SPA-type grid

For apoferritin and ribosome, all the cryo-ET image datasets were acquired using SerialEM, PACEtomo [6] and a cryo-TEM (JEM-3300 (CRYO ARM™ 300 II), JEOL) operated at 300 kV with a K3 direct electron detector (Gatan, Inc.) in the CDS mode. The Ω-type in-column energy filter was operated with a slit width of 20 eV for zero-loss imaging. The magnification was 50,000 ×, with a camera pixel size of 1.01 Å/pixel (physical).

Tilt series were collected using a dose-symmetric tilt scheme using groups of 2 at 3° increments at a defocus range of −2 to −3 μm. For apoferritin, the tilt series were collected between −60° and +60° with a total dose of approximately 137 $e^{-}/Å^{2}$. The tilt images between −36° and +36° were used for data processing. For ribosomes, the tilt series were collected between −60° and +60°, with a total dose of 182 $e^{-}/Å^{2}$. The tilt images between −48° and +36° were used for data processing. Imaging was performed with a total exposure time of approximately 0.4 s at 10 frames/s per tilt angle. Tilt series were simultaneously acquired at 121 sites with an 11 by 11 matrix using PACEtomo [6]. In total, 121 tilt series were collected in about 650 min for each sample.

Reconstruction and subtomogram averaging were performed using Warp/M [7], AreTomo2, and RELION 5.0 [8]. Particle picking was conducted using pytom-match-pick [9] (Supplementary

Figure 1).

For apoferritin, 158,180 particles (box = 86 pixels, binning = 3) were extracted from 121 tomograms and refined iteratively; 154,717 particles were retained after removal of duplicate particles. The reconstructed 3D maps were refined with octahedral symmetry in RELION and further refinements (CTF parameters and tilt image alignment) were performed in M (box = 246 pixels, binning = 1).

For ribosomes, 31,528 particles were extracted from 117 tomograms (box = 100 pixels, binning = 4) and refined iteratively; 26,077 particles corresponding to intact 70S ribosomes were retained after 3D classification and removal of duplicate particles. These 117 tomograms were selected from an initial set of 121 tomograms, with four datasets excluded due to suboptimal tracking performance during tilt-series alignment. The particles were focus-refined using 70S, 50S, or 30S masks in RELION and further refinements (CTF parameters and tilt image alignment) were performed in M (box = 528 pixels, binning = 1). All structural figures were prepared using UCSF ChimeraX [10].

2.4. Lamellae preparation of Salmonella cells for cryo-ET

Salmonella enterica serovar Typhimurium SJW1103 cells were grown in LB medium (1% w/v tryptone, 0.5% w/v yeast extract, and 0.5% w/v NaCl) overnight at 30 °C with shaking. After harvesting 500 µL of culture by centrifugation at 15,000 rpm for 1 min, the cell pellet was resuspended in PBS (137 mM NaCl, 2.7 mM KCl, 10 mM Na_2HPO_4, 1.8 mM KH_2PO_4, pH 7.4) to achieve a final OD_{600} of 1.0. A 3 µL aliquot of the sample was applied to the carbon side of a Quantifoil R1.2/1.3 grid, followed by 2 µL of PBS applied to the metal side, and blotted for 10 s from the metal side before vitrification using an EM-GP plunge freezer (Leica). Lamellae of *Salmonella* cells were prepared using a cryo-FIB-SEM (JIB-4700F, JEOL). The FIB milling conditions were an accelerating voltage of 30 kV with a rough-milling current of 1 nA and a final-polishing current of 30 pA (Table 1). The targeted lamella thickness was 100–150 nm.

2.5. Cryo-ET data collection and STA image analysis of Salmonella lamellae

Data collection was conducted using the same programs and equipment as those used for data collection of SPA-type grids except that the magnification was 30,000 ×, with a camera pixel size of 1.7 Å/pixel (physical). Tilt series were collected using a dose-symmetric tilt scheme between −40° and +70° with groups of 2 at 3° increments starting from a 20° pre-tilt and targeting a defocus range of −3.5 to −5 µm. The total dose was approximately 137 $e^-/Å^2$. From each lamella, tilt series of 19 sites were simultaneously acquired using PACEtomo [6].

Reconstruction and subtomogram averaging were performed using RELION 5, MotionCor3 [11], AreTomo2 [12], and GCtfFind with particle picking by pytom-match-pick. For the lamella that produced the best resolution of ribosome reconstruction by STA, 41,004 ribosome particles were extracted from 19 tomograms (box = 70 pixels, binning = 4) and refined iteratively; 26,077 particles corresponding to intact 70S ribosomes were retained after 3D classification and removal of duplicate particles. The selected particles were reextracted (box = 140 pixels, binning = 2), refined with a 70S ribosome mask and further refinements (CTF parameters and tilt image alignment) were performed in RELION. All structural figures were prepared using UCSF ChimeraX [10] and subtomo2Chimera [13].

Table 1. Milling parameter settings for cryo-FIB-SEM (JIB-4700F).

	Thickness (μm)	Width (μm)	Beam (pA)	Time (min)
Rough	1.5	15	1,000	9
Mill-1	0.8	14	300	4
Mill-2	0.4	13	100	2
Polish-1	0.2	12.5	30	4
Polish-2	0.15	11.5	30	2

3. Results

3.1. Results of STA image analysis of SPA-type samples

First, the STA analysis was performed for tomograms acquired from the SPA-type thin vitreous ice grids of two different biological macromolecular complexes using CRYO ARM^{TM} 300 II (JEOL) to evaluate the quality of tomography data. In addition, stage displacements were measured and analyzed for the Stage X, Y, and Z components using the standard tomography acquisition function implemented in SerialEM (Figure 1B,C). As a result, displacements of approximately −2.5 to +0.5 μm were observed along Stage Y, which is parallel to the tilt axis, while displacements of approximately −1.5 to 0.0 μm were observed along Stage X, which is perpendicular to the tilt axis (Figure 1B). In addition, displacements of approximately −2.5 to +2.0 μm were also observed along the Stage Z direction (Figure 1C). Nevertheless, stable tomographic datasets were successfully acquired using the built-in SerialEM tomography routines even when a dose-symmetric acquisition scheme was employed. Based on these results, we conclude that tomographic data acquisition over an angular range from −60° to +60° using PACEtomo is sufficiently feasible under the conditions used in this study.

Using PACEtomo [6], tomography data collection was performed on a Quantifoil R1.2/1.3 grids in an 11 by 11 matrix. The specimens used were mouse apoferritin and ribosomes from *E. coli*. For both samples, tilt series were collected from −60° to +60° at 3° increments. The total acquisition time for each set of 121 tomograms was approximately 650 min, corresponding to ~5.4 min per tomogram. The ice thickness was 20–30 nm for apoferritin and approximately 50 nm for ribosomes.

By the STA analysis, the apoferritin reconstruction reached a resolution of 2.04 Å (Figure 2A,B, and Supplementary Figure 2) [EMD-67082], and the ribosome reconstruction achieved resolutions of 2.86 Å (70S overall) [EMD-67081], 2.77 Å (focused on 50S), and 2.92 Å (focused on 30S) (Figure 2C,D, and Supplementary Figure 3). The resolution of apoferritin reached close to the Nyquist frequency (2.0 Å), indicating the high optical stability despite a maximum image-shift radius of ~17 μm across the 11 by 11 matrix of holes on the R1.2/1.3 grid. For apoferritin, the holes of six-membered aromatic rings were distinctly resolved (Figure 2B). The resolution of the ribosome was comparable to those obtained with a Krios G4 (Thermo Fisher Scientific) under similar conditions [6], demonstrating equally high stability and reproducibility of tomography data collection using CRYO ARM^{TM} 300 II and PACEtomo. Although the ribosome reconstruction exhibited locally low-resolution in some regions (Supplementary Figure 3), the central core region, which includes the 50S ribosomal protein L20 (Figure 2D), showed good agreement with the fitted atomic model and well-resolved side chains, confirming the reliability of the reconstruction for structural interpretation.

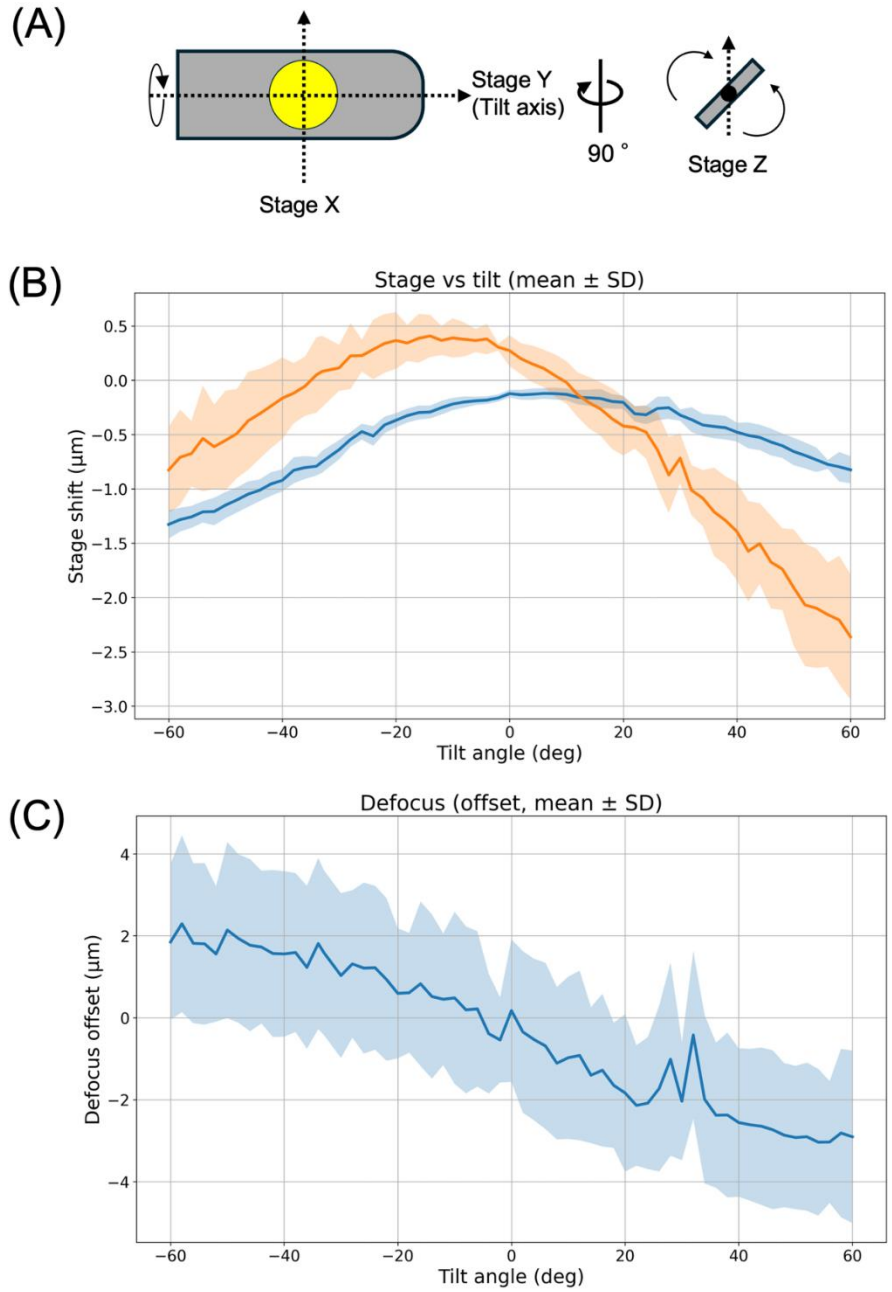

Figure 1. Analysis of stage motion in CRYO ARM 300 II. (A) Schematic illustration of the tilting motion using the cartridge system. The left panel defines the stage coordinate system, showing Stage X and Stage Y. The longitudinal axis of the cartridge corresponds to Stage Y, which is equivalent to the tilt axis during tomography. The orthogonal direction corresponds to Stage X. The right panel shows a front view of the tilt axis, illustrating motion along Stage Z, which corresponds to the specimen height direction. (B) Stage X and Y displacements as a function of tilt angle during tomographic data acquisition using a dose-symmetric scheme. Nine independent tilt series were acquired using the built-in tomography function in SerialEM, and the stage positions were recorded for each series. Mean values and standard deviations (SD) were calculated and plotted against the tilt angle. (C) Changes in the Stage Z component as a function of tilt angle under the dose-symmetric scheme.

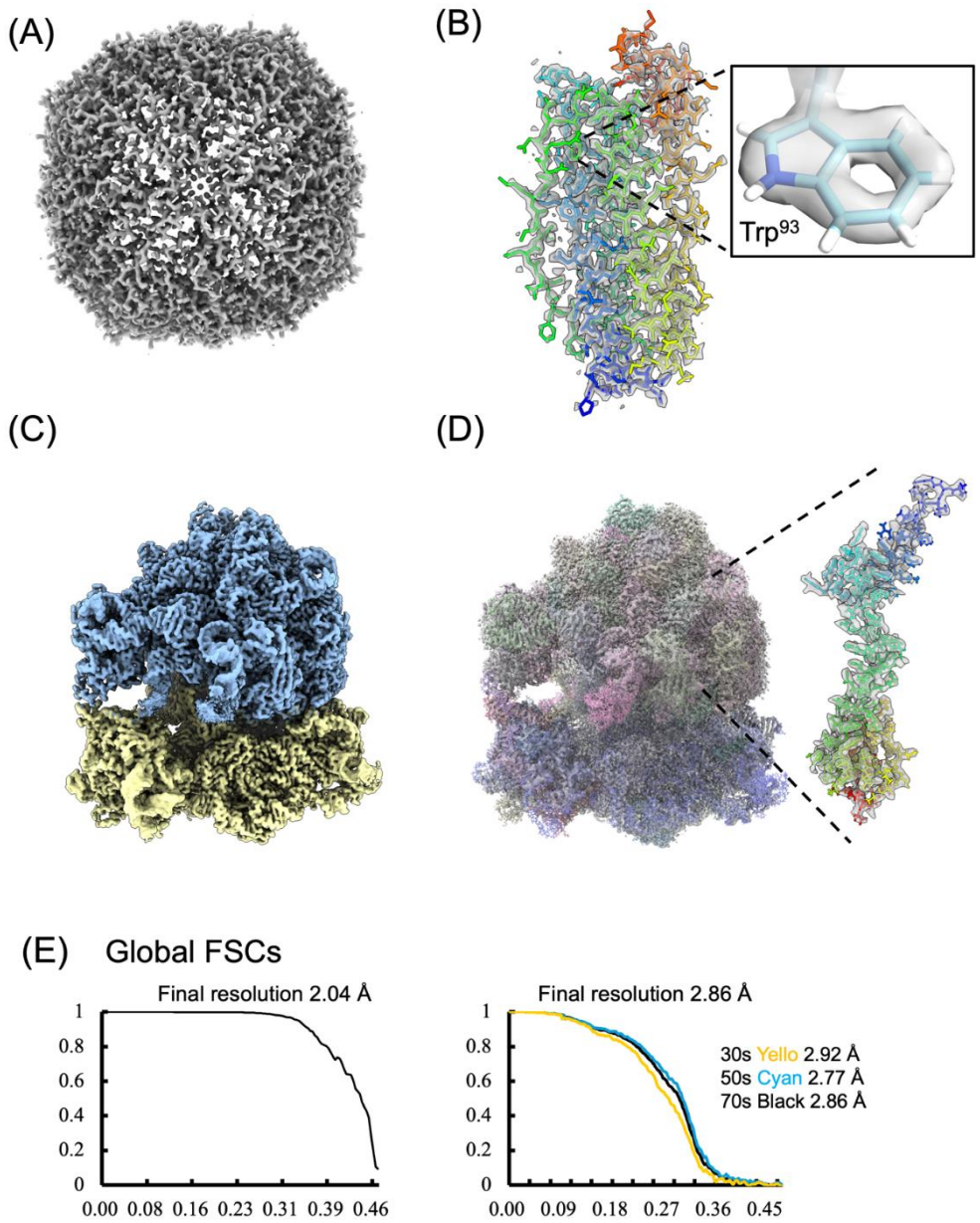

Figure 2. Result of STA data processing for SPA-type grid samples. (A) Subtomogram averaging (STA) reconstruction of apoferritin at 2.04 Å resolution. (B) A single subunit extracted from the assembly and the fitted atomic model is overlaid. The atomic model shows good agreement with the density map, and the central hole of the Trp93 aromatic six-membered ring is clearly visible in the density. (C) STA reconstruction of 70S ribosome at 2.86 Å resolution. Cyan and yellow indicate 50S and 30S ribosome at 2.77 and 2.86 Å resolution, respectively. (D) A 50S ribosomal protein, L20, is extracted and the fitted atomic model is overlaid. (E) The global Fourier shell correlation (FSC) curves of the STA reconstructions: apoferritin (left) and ribosome (right). Resolution was estimated using the gold-standard FSC = 0.143 criterion.

3.2. Results of STA image analysis of cellular lamellae

Tomographic data acquisition was also performed on lamellae of vitrified *Salmonella* cells prepared using a cryo-FIB-SEM system (JIB-4700F, JEOL). Lamella milling was conducted on a single grid, from which 19 lamellae were generated. Among them, five lamellae remained structurally intact and were used for tomographic data collection by PACEtomo. The thicknesses of these lamellae ranged from 80 to 180 nm (Table 2).

Table 2. Lamellae thickness and resolution of ribosome

Lamellae number	Thickness (nm)	Resolution (Å)
1	~110	8.2
2	~170	24.1
3	~130	22.9
4	~180	22.9
5	~80	20.8

Among these five intact lamellae, a lamella with an average thickness of approximately 110 nm was identified as the highest-quality specimen obtained in this study. Tomograms from the other lamellae were not included in the final reconstruction because their inclusion did not lead to any improvement in the achieved resolution (Table 2). A montage image of this lamella clearly revealed densely packed *Salmonella* cells (Figure 3A). From this lamella, 19 tilt series were acquired using PACEtomo, and a total of 26,077 ribosome particles were extracted for subtomogram averaging (STA). Particle picking was performed using pytom-match-pick, and subsequent STA analysis was carried out using RELION 5.0. As a result, a 3D density map of 8.2 Å resolution was obtained from this single lamella (Figure 3B,D, Supplementary Figure 4) [EMD-67083]. Other lamellae yielded ribosome reconstructions with resolutions worse than 20 Å (Table 2). Since combining ribosome particles from these lower-quality lamellae did not lead to any improvement in resolution, they were excluded from the final STA reconstruction. Ribosome particles within a *Salmonella* cell were visualized using ChimeraX by overlaying the reconstructed particles onto the tomographic reconstruction at the coordinates and orientations determined by template matching (Figure 3C).

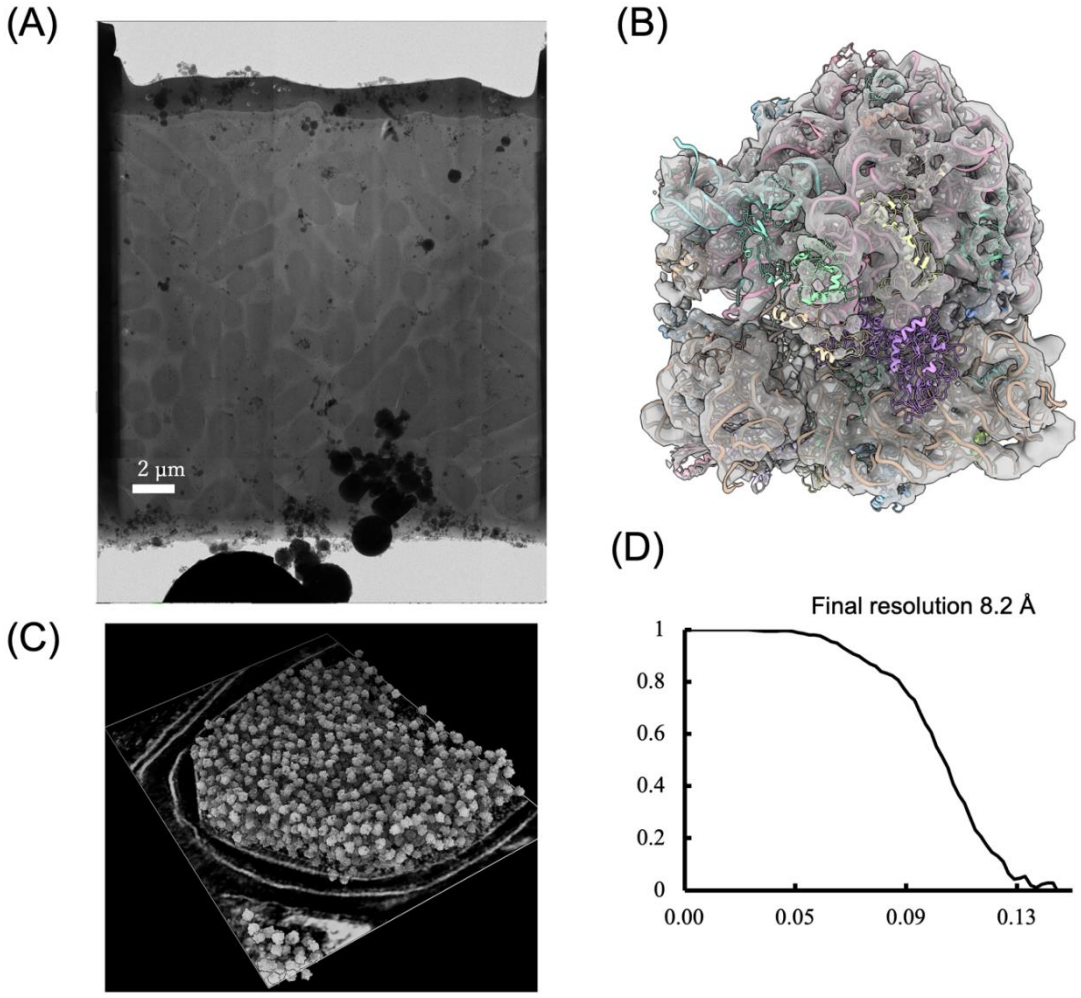

Figure 3. Result of STA data processing for cellular lamella samples. (A) Cryo-electron micrograph of a *Salmonella* lamella specimen. (B) STA reconstruction of *Salmonella* ribosome at 8.2 Å resolution, with the atomic model (PDB ID: 5IMQ) fitted to the density. (C) Visualization of ribosomes inside a *Salmonella* cell using ChimeraX by overlaying the reconstructed ribosome particle on corresponding particle densities in a tomographic reconstruction of the *Salmonella* cell at the coordinates and in the orientations obtained by template matching. (D) The global Fourier shell correlation (FSC) curve of the STA reconstruction.

4. Conclusions

In this study, we systematically evaluated tomographic imaging and subtomogram averaging (STA) using a cryo-TEM, CRYO ARM 300 II, for both SPA-type specimens and cellular lamellae prepared by cryo-FIB-SEM (JIB-4700F).

For SPA-type samples, resolutions of 2.04 Å and 2.86 Å were achieved for apoferritin and the yeast 70S ribosome, respectively, from cryo-ET datasets collected over approximately 11 hours. Analysis of the stage behavior revealed that CRYO ARM^{TM} 300 II exhibited larger displacements than Thermo Fisher Scientific instruments, particularly along the tilt-axis direction (Stage Y), consistent

with previous reports [14,15]. Under the conditions used in this study, we observed displacements of approximately −2.5 to +0.5 μm along the tilt axis, −1.5 to 0.0 μm along Stage X, and relatively large variations in the Stage Z component.

Under such conditions, predictive imaging algorithms such as fast-incremental single-exposure (FISE) are likely difficult to apply [14]. In contrast, tilt-by-tilt tracking corrections implemented in the standard tomography routines of SerialEM and in PACEtomo functioned effectively, ensuring a sufficient tracking performance even in the presence of relatively large stage displacements. As a result, high-resolution structures were successfully obtained by STA analyses of SPA-type grids.

The resolution achieved for apoferritin in this study almost approached the Nyquist limit. Although direct instrument-to-instrument comparisons are not straightforward, the obtained results are comparable to previously reported high-resolution cryo-ET STA studies [16,17]. These findings indicate that, even under conditions where stage-related limitations exist, high-resolution STA analyses can be done efficiently through appropriate tracking corrections and combined use of Warp/M and RELION 5.

For cellular lamella samples, we successfully determined an in situ ribosome structure from *Salmonella* cells at a resolution of 8.2 Å. This result demonstrates that the same instrument configuration and analysis workflow can be applied across a wide range of sample types, from purified specimens to intracellular macromolecular assemblies, enabling both structural identification and analysis at sufficiently high resolutions.

However, for cellular lamellae, the structural determination of ribosome at high resolution was successful in only one out of five lamellae, indicating that reproducibility remains a challenge. The limited resolutions resulted from the other 4 lamellae may be attributed to factors such as insufficient stage tracking accuracy or focus instability at individual tilt angles. Notably, however, such limitations were not observed for the SPA-type samples acquired on the standard grids, suggesting that the reduced contrast and increased complexity inherent to cellular lamellae may have impaired the performance of tracking and focusing algorithms in PACEtomo under certain conditions. In thin lamellae, damage induced by gallium ions has been reported [18] and may have affected the success rate of structural analysis. In addition, multiple factors are likely to have contributed, including suboptimal tracking during tomographic acquisition, ice quality during vitrification, damage introduced during milling, charging effects during imaging (including conductive coating conditions), and limitations in tilt-series alignment accuracy in the absence of fiducial markers. The lack of systematic optimization of these factors represents a limitation of the present study.

Importantly, however, the successful lamella yielded a resolution of 8.2 Å from a single lamella, demonstrating that when imaging and tracking conditions are sufficiently met, the CRYO ARM^{TM} 300 II platform combined with the present workflow is capable of delivering structurally interpretable in situ STA results. The limited success rate therefore reflects the current challenges in lamella preparation and tomographic acquisition rather than a fundamental limitation of the microscope or analysis pipeline.

Use of generative-AI tools declaration

Artificial Intelligence (AI) tools were used solely for language editing and proofreading. No AI tools were used for scientific content generation or data analysis.

Acknowledgments

We thank Radostin Danev for his valuable advice and assistance in setting up and optimizing the PACEtomo system in our CRYO ARM™ 300 II, Yoshie Kushima for help in establishing lamella preparation workflow by cryo-FIB-SEM. We also thank Radostin Danev for his careful reading of the manuscript and for providing insightful and constructive suggestions. This work has been supported by Platform Project for Supporting Drug Discovery and Life Science Research (BINDS) from AMED under Grant Numbers JP24am121003 (to K.N.), by the Cyclic Innovation for Clinical Empowerment from AMED under Grant Number JP17pc0101020 (to K.N.), and by JEOL YOKOGUSHI Research Alliance Laboratories of the University of Osaka (to K.N.).

Conflict of interest

The products (CRYO ARM™) described and utilized in this manuscript are proprietary products of JEOL, the employer of (some of) the authors.

Author contributions

F.M. and K.N. conceptualized, administered, and supervised the project. F.M., and H.Y. and F.E. designed the experiments. T.M, M.K. and H.Y. prepared protein and cell samples. T.M., M.K., F.E., F.M., and H.Y. performed experiments with cryo-FIB-SEM and data collection with a cryo-TEM. H.Y. conducted the STA image analysis. F.M. wrote the initial draft of the manuscript. All authors reviewed, edited, and approved the final version of the manuscript.

References

1. Schur FKM (2019) Toward high-resolution in situ structural biology with cryo-electron tomography and subtomogram averaging. *Curr Opin Struct Biol* 58: 1–9. https://doi.org/10.1016/j.sbi.2019.03.018
2. Obr M, Hagen WJH, Dick RA, et al. (2022) Exploring high-resolution cryo-ET and subtomogram averaging capabilities of contemporary DEDs. *J Struct Biol* 214: 107826. https://doi.org/10.1016/j.jsb.2022.107852
3. Marko M, Hsieh C, Schalek R, et al. (2007) Focused-ion-beam thinning of frozen-hydrated biological specimens for cryo-electron microscopy. *Nat Methods* 4: 215–217. https://doi.org/10.1038/nmeth1014
4. Koning RI, Koster AJ, Sharp TH (2018) Advances in cryo-electron tomography for biology and medicine. *Curr Opin Struct Biol* 52: 1–7. https://doi.org/10.1016/j.sbi.2018.02.007
5. Danev R, Yanagisawa H, Kikkawa M (2021) Cryo-EM performance testing of hardware and data acquisition strategies. *Microscopy* 70: 487–497. https://doi.org/10.1093/jmicro/dfab016
6. Eisenstein F, Danev R, Pilhofer M (2022) Parallel cryo-electron tomography on in situ lamellae. *Nat Methods* 19: 452–459. https://doi.org/10.1038/s41592-022-01690-1
7. Tegunov D, Cramer P (2019) Real-time cryo-EM data preprocessing with warp. *Nat Methods* 16: 1146–1152. https://doi.org/10.1038/s41592-019-0580-y

8. Burt A, Zivanov J, Hagen WJH, et al. (2024) An image processing pipeline for electron cryo-tomography in RELION-5. *FEBS Open Bio* 14: 1788–1804. https://doi.org/10.1002/2211-5463.13967
9. Chaillet ML, Roet S, Veltkamp RC, et al. (2025) Pytom-match-pick: a tophat-transform constraint for automated classification in template matching. *J Struct Biol X* 11: 100125. https://doi.org/10.1016/j.yjsbx.2025.100125
10. Pettersen EF, Goddard TD, Huang CC, et al. (2021) UCSF ChimeraX: structure visualization for researchers, educators, and developers. *Protein Sci* 30: 70–82. https://doi.org/10.1002/pro.3943
11. Zheng S, Wolff G, Greenan G, et al. (2022) AreTomo: an integrated software package for automated marker-free, motion-corrected cryo-electron tomographic alignment and reconstruction. *J Struct Biol* X 6: 100068. https://doi.org/10.1016/j.yjsbx.2022.100068
12. Zheng S, Palovcak E, Armache JP, et al. (2017) MotionCor2: anisotropic correction of beam-induced motion for improved cryo-electron microscopy. *Nat Methods* 14: 331–332 https://doi.org/10.1038/nmeth.4193
13. Bui KH (2022) Builab/subtomo2Chimera v0.12 (0.12). *Zenodo* https://doi.org/10.5281/zenodo.6820119
14. Eisenstein F, Danev R, Pilhofer M (2019) Improved applicability and robustness of fast cryo-electron tomography data acquisition. *J Struct Biol* 208: 107−114. https://doi.org/10.1016/j.jsb.2019.08.006
15. Chreifi G, Chen S, Metskas LA, et al. (2019). Rapid tilt-series acquisition for electron cryotomography. *J Struct Biol* 205: 163−169. https://doi.org/10.1016/j.jsb.2018.12.008
16. Obr M, Hagen WJH, Dick RA, et al. (2022) Exploring high-resolution cryo-ET and subtomogram averaging capabilities of contemporary DEDs. *J Struct Biol* 214: 107852. https://doi.org/10.1016/j.jsb.2022.107852
17. Ni T, Frosio T, Mendonça L, et al. (2022) High-resolution in situ structure determination by cryo-electron tomography and subtomogram averaging using emClarity. *Nat Protoc* 17: 421−444. https://doi.org/10.1038/s41596-021-00648-5
18. Lucas BA, Grigorieff N (2023) Quantification of gallium cryo-FIB milling damage in biological lamellae. *Proc Natl Acad Sci USA* 120: e2301852120. https://doi.org/10.1073/pnas.2301852120

AIMS Press